Investigating the performances of a 1 MV high pulsed power linear transformer driver: from beam dynamics to x radiation

R. Maisonny,* M. Ribière, M. Toury, J. M. Plewa, M. Caron, G. Auriel, and T. d'Almeida
Commissariat à l'Energie Atomique, CEA, DAM, Gramat, F-46500 Gramat, France
(Received 20 September 2016; published 16 December 2016)

The performance of a 1 MV pulsed high-power linear transformer driver accelerator were extensively investigated based on a numerical approach which utilizes both electromagnetic and Monte Carlo simulations. Particle-in-cell calculations were employed to examine the beam dynamics throughout the magnetically insulated transmission line which governs the coupling between the generator and the electron diode. Based on the information provided by the study of the beam dynamics, and using Monte Carlo methods, the main properties of the resulting x radiation were predicted. Good agreement was found between these simulations and experimental results. This work provides a detailed understanding of mechanisms affecting the performances of this type of high current, high-voltage pulsed accelerator, which are very promising for a growing number of applications.

DOI: 10.1103/PhysRevAccelBeams.19.120401

I. INTRODUCTION

Linear transformer driver (LTD) technology [1] is very promising for building compact, versatile and high voltage drivers for various applications, including flash x-ray radiography. Several megavolt prototype drivers based on this technology are being developed around the world for this purpose [2–4]. An LTD driver is a type of inductive voltage adder (IVA) [5] in which the primary energy storage is located inside the IVA cell. Inside the cell, one brick is made of two capacitors discharging through a low inductance spark gap switch. One cavity is composed of a specific number of bricks connected in parallel which determine the desired cavity impedance. In this architecture, a compression stage such as pulse forming line is no longer necessary, the circuit inductance being sufficiently low to allow direct production of a high power electrical pulse with duration less than 100 ns. The pulse shape is mainly determined by both the capacitance and inductance of the cavity. Finally, the cavities are added together in series so that their voltages are summed up, usually along a vacuum coaxial line.

The 1 MV LTD driver was initially built at "Commissariat à l'Energie Atomique" (CEA) as a first module of an 8 MV/48 Ω flash radiography machine [6]. It was successfully tested and was capable of delivering a 1 MV output electrical pulse on a 6 Ω electron beam diode with a full width at half maximum of 75 ns [7]. The ten ultrafast cavities composing the 1 MV LTD are stacked in series as shown in Fig. 1. Each cavity comprises 16 parallel bricks.

The hollow central bore of the ten cavities forms the outer conductor of a long coaxial transmission line. A cathode stalk is inserted into the bore center, forming a magnetically insulated transmission line (MITL) which drives a large area electrons beam diode (LAD) located at its end. Typically, within the diode, electrons are produced and accelerated across the gap toward the anode where they are converted into x rays due to bremsstrahlung. However, in the present configuration a low atomic number (low Z) material anode is used instead in order to minimize the x radiation. Also, unlike nominal radiography diodes, the LAD impedance is roughly constant, as long as ions are not emitted from the anode. Therefore, LAD is a reusable component, well suited for investigating the behavior of the generator.

An accurate understanding and modeling of LTD drivers is crucial for designing future high voltages systems (>1 MV). This work provides a comprehensive numerical analysis of the electron dynamics within the CEA 1 MV LTD machine based on the LSP particle-in-cells (PIC) code [8]. First, the numerical overall simulation setup, which includes the equivalent circuit model and the magnetically insulated transmission line (MITL) geometry, is presented. Next, simulation results are discussed and compared to experimental measurements. Finally, the main concluding remarks about this numerical approach are drawn.

II. SIMULATION SETUP

A. Circuit model

A single LTD cavity is represented by a simplified equivalent circuit model shown in Fig. 2. In this model, the energy storage is simulated by an LRC circuit where L_{cavity} and R_{cavity} are the equivalent capacitance, inductance

*remi.maisonny@cea.fr

FIG. 1. Overall view of the 1 MV driver composed of ten stacked cavities in series.

and resistance of the 16 parallels bricks, respectively. Current losses occurring within the magnetic core are modeled using a constant value resistor (R_{core}) in parallel with the load.

The BERTHA [9] transmission line algorithms were imported into the PIC code LSP, enabling circuits to be coupled directly to LSP electromagnetic wave inlet/outlet boundaries. An outlet boundary is a port which allows electromagnetic waves to exit the simulation space, and optionally allows user-specified waves to enter. The BERTHA circuit model of the LTD was used for each cavity. Several approaches were proposed for improving the modeling of the cavity. Leckbee and co-workers [10] proposed a time dependence for the loss core resistance (R_{core}) in series with the low inductance. Rose and co-workers [11] developed a 3D fully electromagnetic model of the main pulsed-power components within a cavity. Both models have shown good agreement with the simplified circuit model used in the present study.

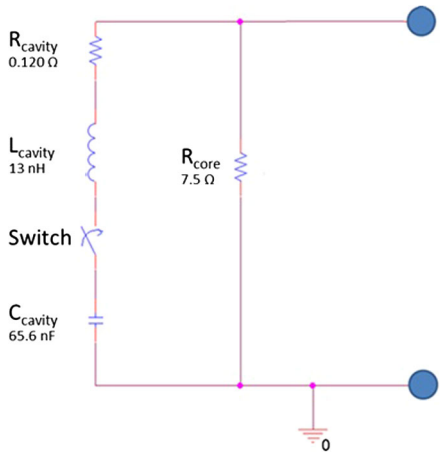

FIG. 2. Simplified circuit model of each LTD cavity. The right part is connected to the LSP grid across the inlet boundary.

B. Geometry

PIC simulations were used to characterize the electron flow within the MITL. The simulations were performed with the fully relativistic 3D-LSP code in 2D cylindrical geometry (R, Z) using a 0.05 cm grid resolution. A parallel computer system using 144 processor cores was utilized to carry out these simulations on approximately 3.4×10^6 grid cells. The same calculations were also performed using the TERA supercomputer with 1920 processor cores (4.0×10^7 grid cells) with a lower grid resolution. This demonstrated the adequacy of the resolution chosen in this work. The 1 MV LTD simulation geometry is shown in Fig. 3.

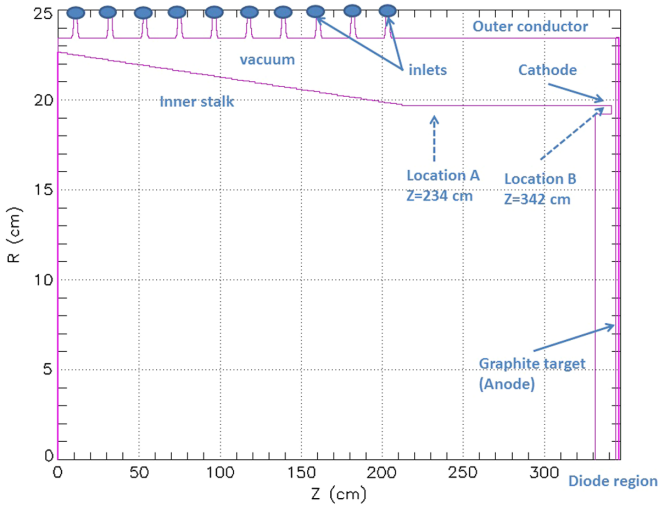

FIG. 3. Geometry used for simulating the 1 MV LTD coupled to the large area diode.

In these simulations, space charge limited (SCL) electron emission [12] was used to generate a sheath current within the transmission line. SCL electron emission was allowed at the cathode when the electric field exceeded 150 kV/cm, while proton emission was allowed at the anode for temperatures exceeding 400 °C based on the study in [13].

The Monte Carlo treatment of electron transport in materials uses the physics kernel of the Integrated Tiger Series (ITS) codes [14], developed by Halbleib and coworkers at Sandia National Laboratories and the National Institute of Standards and Technology. The LSP code was operated with an explicit particle push and a time-biased explicit field solver to damp high frequency noise. The typical time step was 1.06 ps.

III. RESULTS

A. Single cavity

In order to check the electrical properties of a single cavity, an electromagnetic simulation was performed using the LSP code for a particle-free cavity driving a coaxial line. In this simulation, the previous circuit model was used with a ±100 kV charging voltage. This circuit was coupled through an inlet boundary near the gap. The load impedance is determined by the radius of the central stalk. Figure 4 is a comparison between the experimental and simulated output voltages obtained with a 0.6 Ω resistive load.

The amplitude and time profiles of the experimental data are well reproduced by the simulation, with agreement within 5% for the peak voltage. Similar good agreement between simulations and experiments is observed at the same resistance value, in the 0.3 to 0.8 Ω resistive load range.

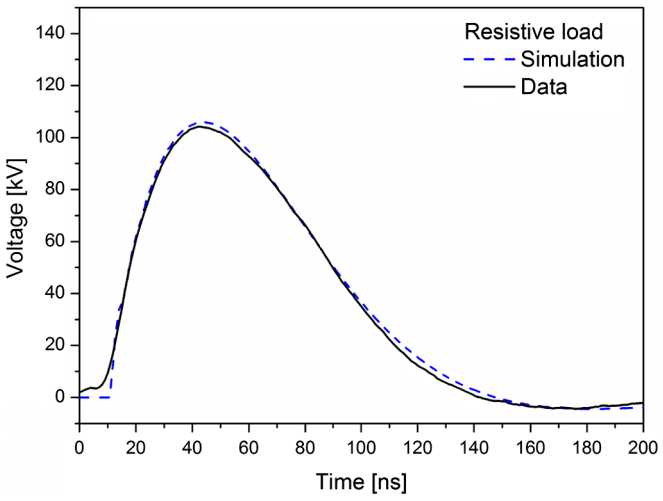

FIG. 4. Comparison of experimental data and simulation (LSP) results for a test of a single LTD cavity with a 0.6 Ω resistive load.

B. Ten cavity generator on a large area diode

A set of experiments was carried out on the 1 MV LTD driver equipped with a large area diode at charging voltages of ±100 kV, with a 24.5 mm axial anode-cathode gap. A direct comparison between simulated and measured transmission line currents and voltages is presented next.

1. Experimental validation of the simulation

Figure 5 shows both the simulated and experimental anode (Rogowsky) and cathode currents (B-dots) at the end of the tenth cavity, corresponding to location A in Fig. 3. The outer anode current represents the total current in the line. The cathode current corresponds to the current flowing through the cathode and does not include electrons flowing in vacuum (sheath current).

Beyond the last cavity, at location A in Fig. 3, and at the time of peak power, the simulated and experimental smoothed total current are 179.4 and 175.8 kA, respectively. As can be seen in Fig. 5, the agreement between simulated and experimental anode and cathode currents is rather satisfactory, considering that differences in triggering time between cavities (±5 ns) are not taken into account in the simulations. At a specific time, slightly different from simulation to experiment, a rapid increase of the cathode current is observed while the sheath current decreases. This is characteristic of some retrapping of the sheath electron current into the cathode. This retrapping wave likely results from the impedance mismatch between the generator and the load. Current retrapping in MITLs was examined in Ref. [15]. These studies show that when such retrapping occurs, the voltage can no longer be accurately determined using the Mendel method [16] based on the anode to cathode currents ratio. However, this discrepancy does not significantly affect the accuracy of the inferred MITL

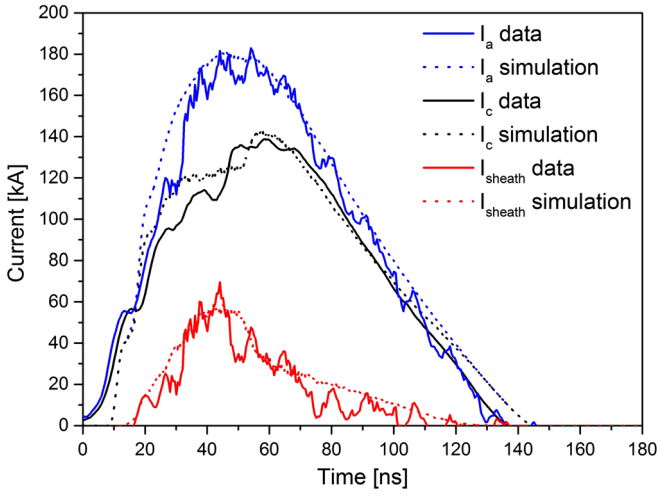

FIG. 5. Simulated and experimental anode, cathode and sheath currents at the end of the tenth cavity (location A on Fig. 3) for a 24.5 mm gap LAD.

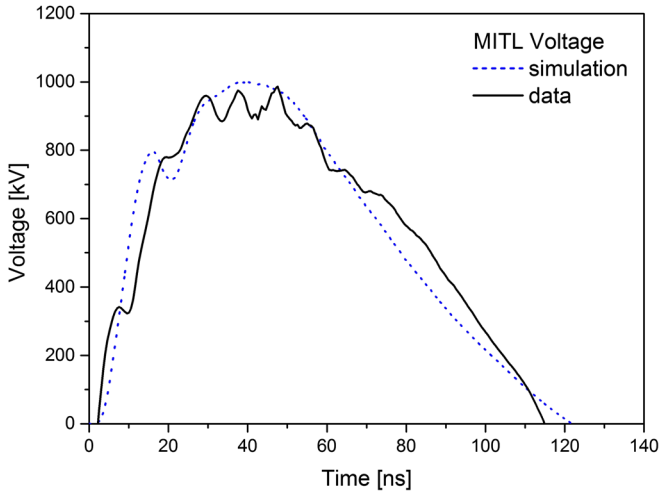

FIG. 6. Comparison of experimental data and simulation results of the MITL voltage after the tenth cavity.

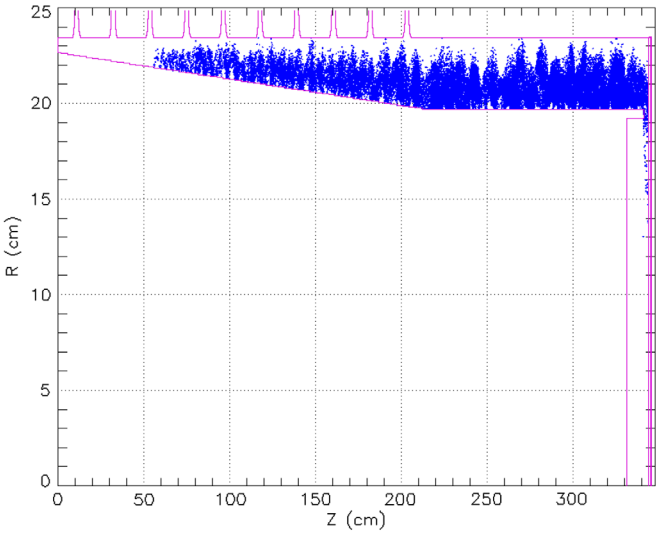

FIG. 7. Electron particle (in blue online) plot at maximum diode peak voltage ($t = 47$ ns) for a LAD with a 24.5 mm d_{AK}.

voltage, since the impedance mismatch is small in this case. Therefore a satisfactory value of the MITL voltage can be obtained after the tenth cavity, based on the Mendel method as shown in Fig. 6.

A more accurate measure of the MITL voltage remains a quite challenging task. Therefore, the approach used here appears to be a reasonable estimate of the voltage, given the approximations that were made. Other factors such as the electron emission threshold and the jitter between cavities are very likely to induce an overshoot during the rise front of the voltage profile, as observed in Fig. 6. Beyond ~55 ns, the discrepancy may be attributed to the limitation associated with the Mendel when retrapping occurs.

2. *Electron flow dynamics*

A good understanding of the electron dynamics is essential for predicting the performance of the transmission line and for analyzing the experimental data. Figure 7 is a (R, Z) cross sectional view of the simulated electron particles within a 24.5 mm gap LAD at peak power, showing electron emission starting right after the third cavity. At first appearance, a large region within the transmission line appears to be filled by an electronic cloud, suggesting poor insulation. However, since macroparticles have different weights depending on the charge they carry, this visualization can only be well understood if the corresponding charge density is also considered.

Figure 8 shows an averaged charge density across R at $t = 47$ ns, over a wide Z-range with constant radius (between $z = 210$ cm and $z = 310$ cm).

As can be seen in Fig. 8, PIC simulations suggest significant changes in charge density as a function of radius. The maximum charge density is obtained near the cathode (inner diameter, $R = 19.7$ cm).

Most analytical MITL models are based on various charge density distribution hypotheses. For example, Miller and co-workers [17] assume that the charge density $\rho(R)$ is uniform across the electron layer from the cathode to the layer edge. In order to provide a more accurate description of equilibrium magnetically insulated flow theory, Ottinger and co-workers [18] removed the assumption on electron density uniformity, and instead, introduced a scaling factor matching the particle in cell simulations. Despite all these improvements, PIC simulations remain the only method capable of properly incorporating impedance transitions within MITLs, cavity voltage transitions in LTD systems, or retrapping waves whenever they are created along the line.

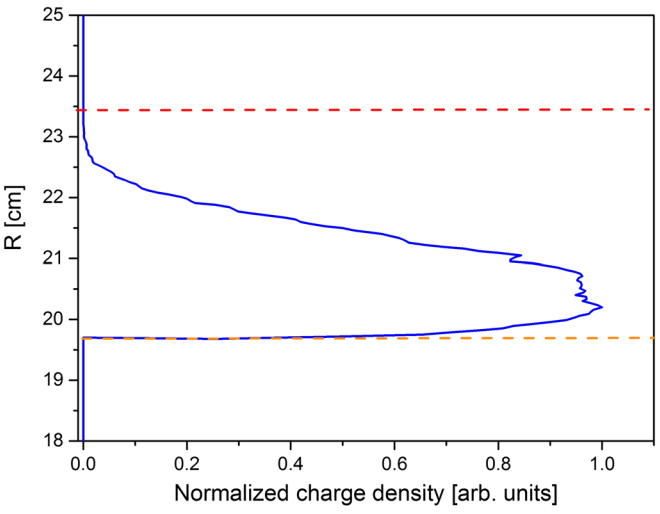

FIG. 8. Normalized average charge density for Z ranging from 210 to 310 cm at $t = 47$ ns. The dotted orange and red lines represent the inner and outer radii of the MITL, respectively.

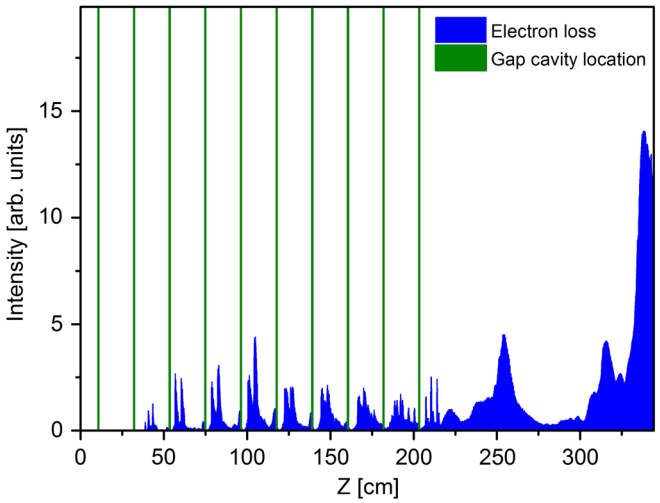

FIG. 9. Calculated time-integrated electronic losses occurring throughout the transmission line. The green lines represent the center of the accelerating gap of each cavity.

3. Electron loss analysis inside the MITL

In order to improve the efficiency of future high pulsed power systems using MITLs, it is important to gain insight into the physical mechanisms responsible for electrons loss occurring during power transfer, whenever electrons hit the outer radius of the line [19]. Hence, in the present simulations, all particles intercepting the line's outer radius located at $R = 23.45$ cm were extracted and analyzed for all Z values. As shown in Fig. 9, electronic losses occur throughout the line, except near the first two cavities, where the electric field intensity is not high enough to initiate electron emission.

It appears that electron losses are not uniformly distributed across the line; 75% of them occurs beyond the tenth cavity for $Z > 210$ cm, mostly near the diode. Furthermore, within the upstream region of the line ($Z < 210$ cm), where losses are relatively low, they are localized between the accelerating gaps. Therefore, very few electrons are likely to impact the vacuum insulators, thus, decreasing the probability of electrical breakdown.

The energy dissipated within the outer diameter and the target due to electronic losses induces a temperature rise, ΔT. This temperature rise is calculated from the energy deposited per unit depth (dE/dx) by each impacting electron, based on the formula

$$\Delta T = \frac{dE}{dx} * \frac{q}{e\rho N_a C_p \cos\theta},$$

where q is the electron charge, ρ is the material density, N_a is the Avogadro's number, θ is the electron's incidence angle and C_p is the material specific heat. Figure 10 represents a 2D plot of the surface temperature rise for the 1 MV LTD at the end of the pulse ($t = 200$ ns).

Electrons impacting the outer diameter of the line do not significantly contribute to the temperature rise. The electrons impacting the outer diameter of the line give a negligible temperature rise (<20 K). At the target surface, the temperature increase reaches a peak value of 90 K. Hence the maximum temperature at the target surface remains below the proton emission threshold of 400 °C. The temperature profile on the target is shown in Fig. 10(b). This profile partly reflects the beam distribution from simulation as shown in Fig. 11.

The output of the simulation is consistent with observations made at the target surface after over 2000 shots as can be seen in the picture inserted in Fig. 11, where target damage is visible at large radius.

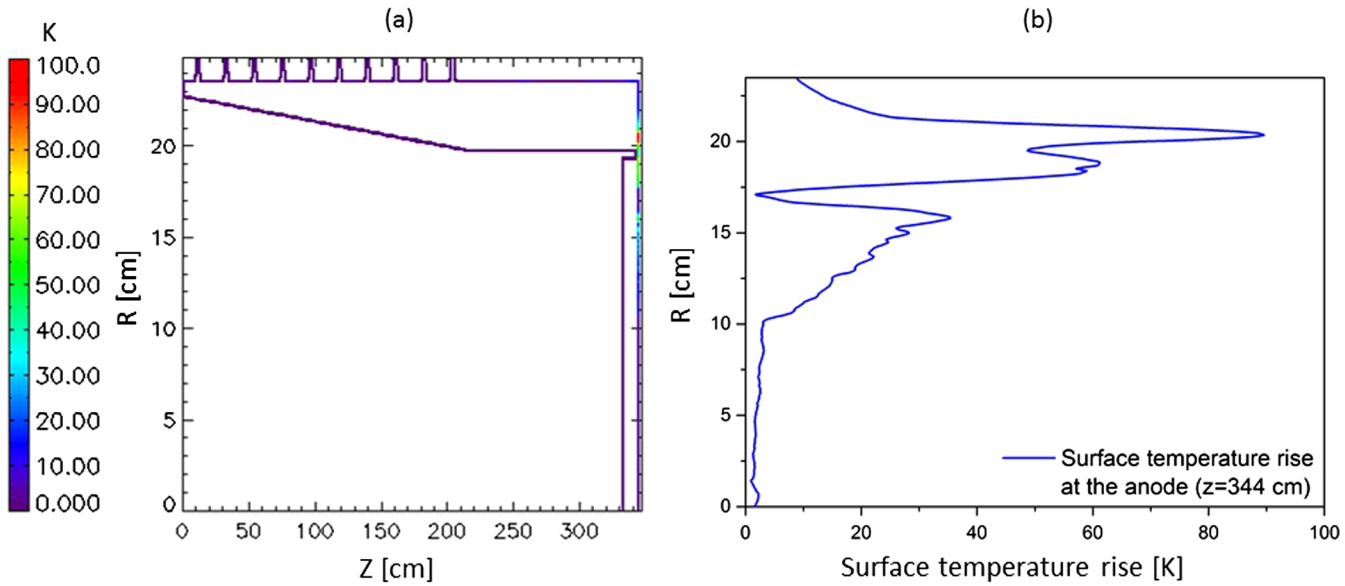

FIG. 10. (a) Simulated surface temperature rise inside the LTD. (b) Simulation of the radial profile of the temperature rise at the surface of the graphite target.

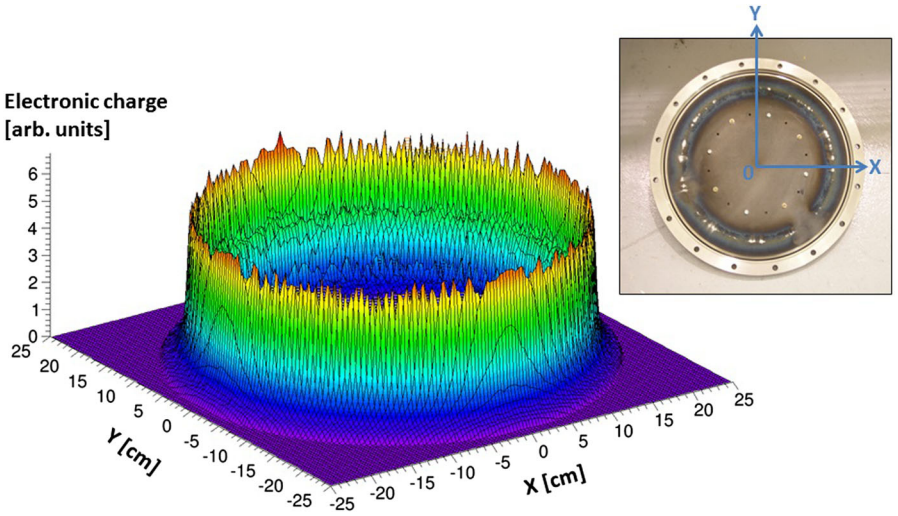

FIG. 11. 3D plot of the beam distribution at the target plane (in Cartesian coordinates). The image on the right is a picture showing wear on the graphite target after more than 2000 shots LAD. Target damage is visible primarily at large radius ($R \sim 20$ cm).

The total charge loss along the outer conductor represents 3.98 mC, while the accelerated electrons impacting the anode carry 12.65 mC. Hence the electron loss represents about 31.5% of the accelerated charge. The time profile associated with electron loss, after integration along z, may be divided into three phases referred to as 1, 2 and 3 and separated by the red dashed line in Fig. 12.

The first phase, which takes place between $t = 0$ ns and $t = 22$ ns, is characterized by a rapid increase of electron loss. During this phase, the MITL current increases (i.e. the number of electrons) but the self-magnetic fields inside the gap are not sufficient to insulate the electrons emitted from the cathode. In the second phase, from 22 to 89 ns, electron loss decreases quickly while the anode current remains relatively high, even though the current decreases significantly for $t > 60$ ns. In this phase, the magnetic fields are sufficiently strong to insulate the sheath current. Very little current loss occurs across the MITL at maximum voltage. In the last phase, after 89 ns, the current keeps decreasing while electron loss is sharply enhanced due to insufficient magnetic insulation. This explanation is supported by the fact that the MITL currents (i.e. the magnetic fields) which delimit the three phases are similar as evidenced by the intersection between the dashed boundary lines in red and the anode current curve.

Figure 13 shows the time-integrated distribution of the electron energy. Most of the "lost" electrons have energies below 600 keV (outer diameter curve). This distribution confirms that the MITL is well insulated at maximum voltage.

In order to examine a possible correlation between the electron energy and the location at which the losses occur

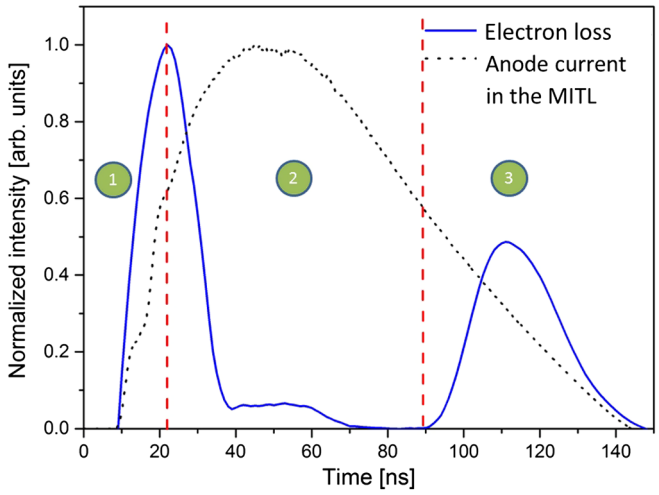

FIG. 12. In blue, temporal evolution of the electrons impacting the outer diameter of the MITL (at $R = 23.45$ cm) integrated across z. In black, temporal evolution of the normalized anode current in the MITL after the tenth cavity.

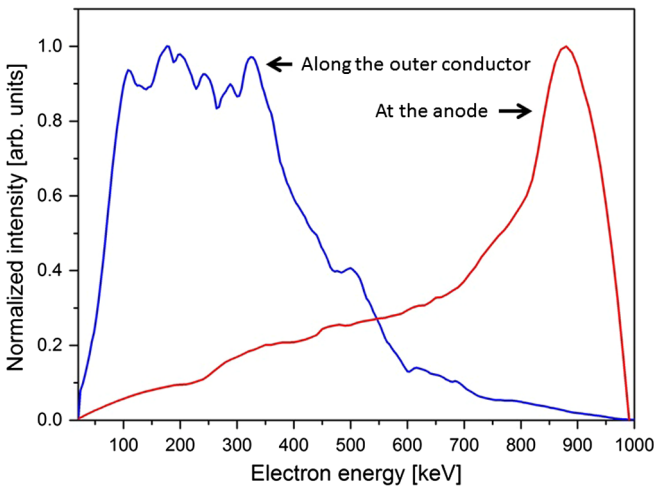

FIG. 13. Comparison of the electron energy distribution of the loss electrons (in blue) and the electron energy distribution inside the diode (red).

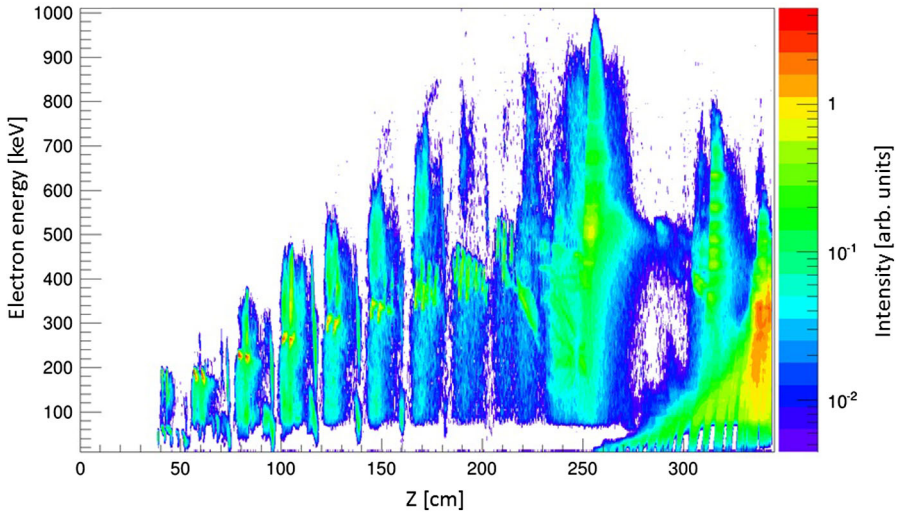

FIG. 14. Time-integrated correlation map between the electron energy and their position along Z after the electrons reached the outer conductor.

within the MITL, we have built a time integrated correlation map (Fig. 14).

Upstream from the tenth cavity ($Z < 210$ cm), the electron energy increases with Z. This results from the gradual energy increase induced by the cavity voltage addition. Most of the losses occur after the tenth cavity. High-energy electron loss, above 600 keV, occurs at $Z = 250$ cm. In addition, a large number of low energy electrons are lost at the end of the line near the diode.

4. Monte Carlo calculation of electron and photon transport in the anode

In this section, the results of Electre-Phoebus 3D Monte Carlo transport simulations are presented [20–21]. This calculation incorporates all the microscopic interactions occurring as the primary e-beam interacts with the solid anode target: collisional ionization and bremsstrahlung, which are the sources of electron energy loss, and also photoelectric and Compton ionization induced by the photons (resulting from bremsstrahlung and, in a lesser proportion fluorescence and electrons-positron creation) which are the source of electron creation. Figure 15 shows the energy distribution of the photons resulting from the transport of the electrons and photons in the anode, which are produced by the electrons incident upon the target. The properties of these incident electrons are predicted from the PIC simulation. One example of such properties is given by the electron energy distribution in Fig. 13.

After the conversion target, the mean photon energy is 270 keV (Fig. 15). It is important to note that photon sources with hundreds of keV are well suited for flash radiography of low Z objects with small areal mass. In this case, the significant difference between material absorption coefficients results in higher contrast in radiographic images. The time integrated photon flux spatial distribution, downstream from the target, is shown in Fig. 16.

Based on the time integrated photon flux spatial distribution and on the flux-to-dose conversion factor (which is 1.3×10^{-12} Gy(air)/(photons/cm^2)), a mapping of the dose in air can be inferred from the photon flux distribution in Fig. 16. Here the on-axis dose in air at 1 m is 0.22 rads. Also, the on-axis dose associated with the radiation induced by electrons impacting the outer diameter of the line, was determined. A negligible dose value of 4×10^{-3} rads was found, which strongly suggests, despite representing 31.5% of the total electronic charge, the loss contribution to the dose is small. Using thermoluminescent dosimeters, an averaged value of the time-integrated dose was obtained over a large number of experiments. The agreement between simulated and experimental on-axis dose at 1 m in air is better than 20%. This good agreement validates the computational models developed in this work for predicting the machine behavior, including higher voltage operation.

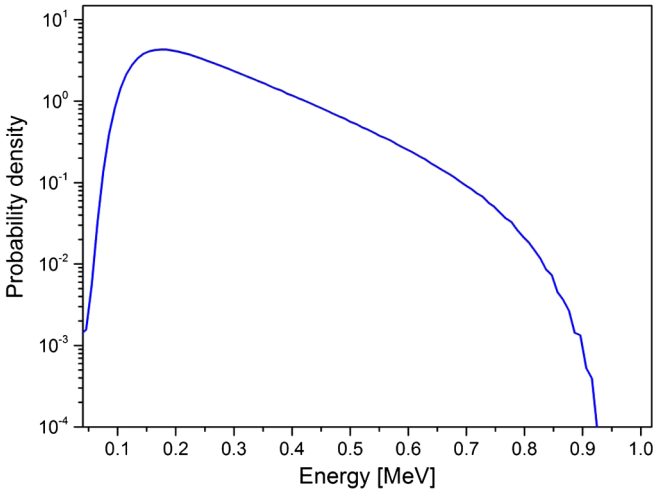

FIG. 15. Time integrated photon energy distribution function behind the conversion target.

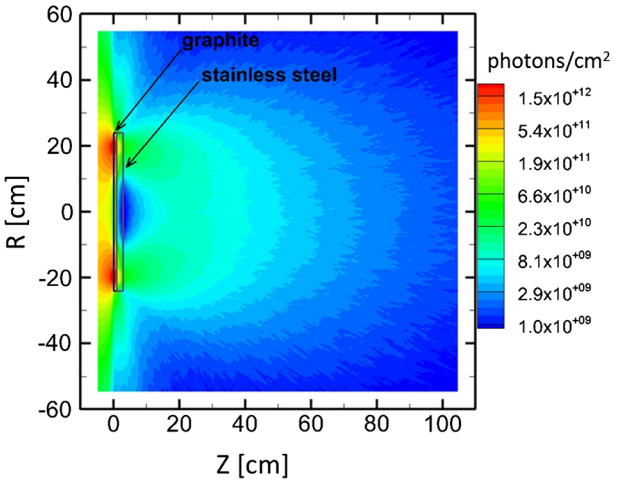

FIG. 16. Photon flux spatial distribution downstream from the target.

IV. CONCLUSION

In this paper, the operation of a single LTD cavity was first modeled by a simplified equivalent circuit, which was adjusted in order to accurately reproduce the experimental data. This model was extended to the ten cavities composing the entire generator, and used as an input to the PIC electromagnetic simulations in order to investigate and to characterize the coupling between the cavities and the MITL. Based on the comparison with various electrical measurements, the electrical performance appeared to be properly reproduced in terms of both the sheath and cathode currents. Also, these simulations provided a reasonable estimate of the MITL voltage, which remains a challenging measurement to achieve, especially when retrapping mechanisms take place. Also, particle-in-cell calculations were employed to examine the beam dynamics within the MITL, providing insight into the electronic losses affecting the performances of the system. Based on the information provided by the study of the beam dynamics, and using Monte Carlo methods, the main properties of the resulting x radiation were predicted. Good agreement was found between these simulations and experimental results. This good agreement validates the computational models developed in this work for predicting the machine behavior, including higher voltage operation. These results confirm the readiness of LTD technology for applications in x-ray flash radiography applications.

ACKNOWLEDGMENTS

Stéphanie Cartier and Frédéric Cartier are thanked for their assistance with the experiments.

[1] A. A. Kim, A. N. Bastrikov, S. N. Volkov, V. G. Durakov, B. M. Kovalchuk, and V. A. Sinebryukhov, Development of the ultra-fast LTD stage, in *Proceedings of the 14th IEEE International Conference in High-Power Particle Beams* (IEEE, Albuquerque, 2002), Vol. 1, pp. 81–84.

[2] A. A. Kim, A. N. Bastrikov, S. N. Volkov, V. G. Durakov, B. M. Kovalchuk, and V. A. Sinebryukhov, 1 MV ultra-fast LTD generator, in *Digest of Technical Papers on the 14th IEEE International Pulsed Power Conference* (IEEE, Dallas, 2003), Vol. 2, pp. 853–854.

[3] J. Leckbee, J. Maenchen, S. Portillo, S. Cordova, I. Molina, D. L. Johnson, and D. Ziska, Reliability assessment of a 1 MV LTD, in *Proceedings of the 15th IEEE International Conference in High-Power Particle Beams* (IEEE, St. Petersburg, 2005), Vol. 1, pp. 132–134.

[4] M. Toury, F. Cartier, P. Combes, S. Cartier, R. Maisonny, M. Caron, and B. Etchessahar, Transfer and test of a 1 MV LTD generator at CEA, in *Proceedings of the 19th IEEE International Pulsed Power Conference* (IEEE, Piscataway, 2013), Vol. 1, pp. 1–4.

[5] I. D. Smith, Induction voltage adders and the induction accelerator family, Phys. Rev. ST Accel. Beams **7**, 064801 (2004).

[6] M. Toury, C. Vermare, B. Etchessahar, L. Veron, M. Mouillet, F. Bayol, and A. A. Kim, IDERIX: An 8 MV flash x-rays machine using a LTD design, in *Proceedings of the 16th IEEE International Pulsed Power Conference* (IEEE, Albuquerque, 2007), Vol. 1, pp. 599–602.

[7] F. Bayol, F. Cubaynes, R. Delplanque, P. Genez, C. Legras, M. Parzych, M. Toury, M. Caron, M. Mouillet, and A. A. Kim, Development of a 1 MV ultra-fast LTD generator, in *Proceedings of the 18th IEEE International Pulsed Power Conference* (IEEE, Chicago, 2011), Vol. 1, pp. 619–624.

[8] LSP is a product of Mission Research Corp., Albuquerque, NM.

[9] D. D. Hinshelwood, Naval Research Laboratory Memorandum Report No. 5185, 1983.

[10] J. Leckbee, S. Cordova, B. Oliver, D. L. Johnson, M. Toury, R. Rosol, and B. Bui, Testing of a 1-MV linear transformer driver (LTD) for radiographic applications, in *Proceedings of the 17th IEEE International Pulsed Power Conference* (IEEE, Washington, 2009), Vol. 1, pp. 156–160.

[11] D. V. Rose, C. L. Miller, D. R. Welch, R. E. Clark, E. A. Madrid, C. B. Mostrom, W. A. Stygar, K. R. LeChien, M. A. Mazarakis, W. L. Langston, J. L. Porter, and J. R. Woodworth, Circuit models and three-dimensional electromagnetic simulations of a 1-MA linear transformer driver stage, Phys. Rev. ST Accel. Beams **13**, 090401 (2010).

[12] I. Langmuir and K. Blodgett, Currents limited by space charge between coaxial cylinders, Phys. Rev. **22**, 347 (1923).

[13] T. W. L. Sanford, J. A. Halbleib, J. W. Poukey, A. L. Pregenzer, R. C. Pate, C. E. Heath, R. Mock, G. A. Mastin, D. C. Ghiglia, T. J. Roemer, P. W. Spence, and G. A. Proulx, Measurement of electron energy deposition necessary to form an anode plasma in Ta, Ti, and C for coaxial bremsstrahlung diodes, J. Appl. Phys. **66**, 10 (1989).

[14] J. A. Halbleib, R. P. Kensek, T. A. Mehlhorn, G. D. Valdez, S. M. Seltzer, and M. J. Berger, ITS: the integrated TIGER series of electron/photon transport codes-Version 3.0, IEEE Trans. Nucl. Sci. **39**, 1025 (1992).

[15] V. L. Bailey, P. A. Corcoran, D. L. Johnson, I. D. Smith, J. E. Maenchen, K. D. Hahn, and B. V. Oliver, Re-trapping of vacuum electron current in magnetically insulated transmission lines, in *Proceedings of the 15th IEEE International Conference in High-Power Particle Beams* (IEEE, St. Petersburg, 2004), pp. 247–250.

[16] C. W. Mendel, D. B. Seibel, and S. E. Rosenthal, A simple theory of magnetic insulation from basic physical considerations, Laser Part. Beams **1**, 311 (1983).

[17] P. A. Miller and C. W. Mendel Jr., Analytic model of Applied-B ion diode impedance behavior, J. Appl. Phys. **61**, 529 (1987).

[18] P. F. Ottinger and J. W. Schumer, Rescaling of equilibrium magnetically insulated flow theory based on results from particle-in-cell simulations, Phys. Plasmas **13**, 063109 (2006).

[19] D. V. Rose, E. A. Madrid, D. R. Welch, R. E. Clark, C. B. Mostrom, W. A. Stygar, and M. E. Cuneo, Computational analysis of current-loss mechanisms in a post-hole convolute driven by magnetically insulated transmission lines, Phys. Rev. ST Accel. Beams **18**, 030402 (2015).

[20] Electre-Phoebus 3D Monte Carlo is a product of *Sigma Plus*.

[21] M. Ribiere, S. Demarquay, M. Maulois, R. Maisonny, T. d'Almeida, M. Toury, B. Crabos, C. Gonzalez, A. Garrigues, C. Delbos, and B. Azais, Contribution of electromagnetic perturbation to the transient response of an electronic circuit exposed to a high multi-MeV X-ray flux, Trans. Nucl. Sci. **62**, 1383 (2015).